List of Publications:

1. **Nilu V. Gone**, Mohammed G. Enayathullah, Jessie Thomas, Parth Rathee, Rajeev Prabhakar, Kiran K. 2023, volume 20, Issue 12, Bokara, Gangadhar J. Sanjayan, "Discovery of SARS-CoV-2 Inhibitors Featuring Novel Histidine α-Nitrile Motif" *Chem. Biodiversity.*, **2023**, *20*, 12, e202300957 (DOI: https://doi.org/10.1002/cbdv.202300957)

2. **Nilu V. Gone**, Tanisha Sharma, Rakesh Joshi, Manas Santra, Gangadhar J. Sanjayan, "Repurposed Ciprofloxacin Derivatives as Potent Autophagic-type Anticancer Agents". (*Under revision in Bioorganic & Medicinal Chemistry Letters*, **2024**)

List of Patents:

1. **Nilu V. Gone,** Kiran Bokar, G. J. Sanjayan, "SARS-COV-2 Inhibitors and Method of Preparation Thereof" 0051NF2024/IN, **2021**. (*Patent Filed*)

2. **Nilu V. Gone** and G. J. Sanjayan, "Ciprofloxacin-Based Autophagic-Type Anticancer Agents" 0139NF2024/IN, **2023**. (*Patent Filed*)

Research Article

Discovery of SARS-CoV-2 Inhibitors Featuring Novel Histidine α-Nitrile Motif

Nilu Vijay Gone,[a, b] Mohammed Ghalib Enayathullah,[c] Jessie Thomas,[c] Parth Rathee,[d] Rajeev Prabhakar,*[d] Kiran Kumar Bokara,*[c] and Gangadhar J. Sanjayan*[a, b]

As COVID-19 infection caused severe public health concerns recently, the development of novel antivirals has become the need of the hour. Main protease (M^{pro}) has been an attractive target for antiviral drugs since it plays a vital role in polyprotein processing and virus maturation. Herein we report the discovery of a novel class of inhibitors against the SARS-CoV-2, bearing histidine α-nitrile motif embedded on a simple dipeptide framework. In-vitro and in-silico studies revealed that the histidine α-nitrile motif envisioned to target the M^{pro} contributes to the inhibitory activity. Among a series of dipeptides synthesized featuring this novel structural motif, some dipep-

tides displayed strong viral reduction ($EC_{50} = 0.48\ \mu M$) with a high selectivity index, $SI > 454.54$. These compounds also exhibit strong binding energies in the range of −28.7 to −34.2 Kcal/mol. The simple dipeptide structural framework, amenable to quick structural variations, coupled with ease of synthesis from readily available commercial starting materials are the major attractive features of this novel class of SARS-CoV-2 inhibitors. The histidine α-nitrile dipeptides raise the hope of discovering potent drug candidates based on this motif to fight the dreaded SARS-CoV-2.

Introduction

SARS-CoV-2 is a deadly pandemic agent that has rapidly infected more than half a billion people across the globe causing unprecedented loss of life and economy.[1] The 'SARS-CoV-2 pandemic', has also become one of the biggest public health catastrophes in contemporary times. The infectious agent of COVID-19, severe acute respiratory syndrome coronavirus 2 (SARS-CoV-2), is an enveloped single-stranded RNA virus of the genus Betacoronavirus belonging to the Coronaviridae family.[2–4] Substantially, a new variant with a detrimental change in the spike would neutralize the vaccine's activity and expose humans to more epidemic threats in the future.[5] SARS-CoV,[6] first reported in 2003, shares 78% genetic similarity with the COVID-19 etiological agent SARS-CoV-2.[7] Owing to the

possibility of recurrent mutations evading currently developed vaccines, there is an urgent need to develop effective SARS-CoV-2 antivirals.[8]

SARS-CoV-2 viral nucleocapsid is endowed with one of the largest genomic RNAs (~30kb).[9] PL^{pro} (Papain-like protease) and $3CL^{pro}$ or M^{pro} (Main protease) perform the cleavage activity of polyprotein - a crucial step for the replication of the virus.[10] The biology and pathogenesis studies of novel coronaviruses emphasized that M^{pro} is a conserved enzyme among all coronaviruses and plays a key role in RNA replication[11] and pathogenesis pathways, and thus it is a potential target for developing novel antiviral candidates. SARS-CoV-2 M^{pro} belongs to the cysteine protease class featuring two protomers which upon dimerization and activation assume appropriate conformation to implement the catalytic functions.[12] Resembling to other cysteine proteases, each protomer is divided into three domains (I, II and III), and its active catalytic dyad is embedded between the cleft of domain II and III of amino acid Cys145 and His41.[13] Homodimerization of the M^{pro} is an essential step for catalytic action because the N-finger of each of the two protomers interacts with Glu166 of the other protomer and thereby creating the appropriate conformation of the S1 pocket of the substrate-binding site.[14] Recent studies have revealed that the antiviral target M^{pro} is safe because no human protease has a similar cleavage affinity for the substrate.[15–17]

Although vaccination can temporarily halt the progression of the COVID-19 pandemic, the most effective and long-term solution to fight SARS-CoV-2 is to develop efficient drug candidates.[18] Since 2019, numerous publications and patents have been filed worldwide based on the identification of new chemical entities, and innumerable available drugs have been evaluated for repurposing as an easy therapeutic strategy for COVID-19.[19–23]

Several M^{pro} inhibitors have been reported recently to specifically bind covalently to Cys145 with a variety of warhead

[a] N. Vijay Gone, Prof. Dr. G. J. Sanjayan
Organic Chemistry Division
CSIR-National Chemical Laboratory
Dr. Homi Bhabha Road, Pune-411008, India

[b] N. Vijay Gone, Prof. Dr. G. J. Sanjayan
Academy of Scientific and Innovative Research (AcSIR)
Ghaziabad, 201002, India
E-mail: gj.sanjayan@ncl.res.in

[c] M. Ghalib Enayathullah, J. Thomas, Prof. Dr. K. Kumar Bokara
Annexe-II, Medical Biotechnology Complex
CSIR-Centre for Cellular and Molecular Biology
Uppal Road, Hyderabad, Telangana, 500007, India
E-mail: bokarakiran@ccmb.res.in

[d] P. Rathee, Prof. Dr. R. Prabhakar
Department of Chemistry
University of Miami
Coral Gables, FL, USA
E-mail: rpr@miami.edu

groups such as: α-ketoamides, α,β-unsaturated ketones, aldehydes, nitrile, etc.[24,25] Structural modification of the potent drug candidate 2 and its related aldehyde 3 led to the discovery of water-soluble prodrug 1 (PF-07304814). Extensive structural modifications on the earlier clinical candidate lufotrelvir further led to the development of nirmatrelvir – a potent antiviral medication developed by Pfizer, which is marketed as Paxlovid – in combination with ritonavir (Figure 1, *vide infra*).[26,27]

In this paper, we report a novel class of short peptides featuring histidine α-nitrile motif and their inhibitory activity against wild-type (WT) SARS-CoV-2.[28] Nine short peptides, carrying histidine α-nitrile motif, were synthesized having diverse structural modifications on the peptide backbone. All peptides were tested for their antiviral potency and comparisons were made of their activity profile with results obtained from *in-silico* studies. *In-vitro* screening suggested that dipeptides featuring this novel histidine α-nitrile motif exhibited antiviral activity and corresponding molecular dynamics simulation studies revealed promising ability to specifically target M^{pro} binding pockets. (Crystal structure PDB ID: 7ALH).

Results and Discussion

The rationale for histidine α-nitrile motif design: M^{pro}, a class of highly conserved cysteine proteases found in CoVs that plays an indispensable role in viral replication, is capable of cleaving polyproteins at nearly eleven sites with three times more cleavage affinity compared to PL^{pro}.[29] The substrate binding site S1 pocket of each protomer is located between the gaps of two of their three domains and features the Cys145-His41 catalytic dyad. The thiol group of Cys145 acts as a nucleophile that could attack on electrophilic carbonyl group of amide linkage of substrate polyproteins and the histidine acts as a general base for transfer of proton generating the acyl-enzyme complex thus resulting in the
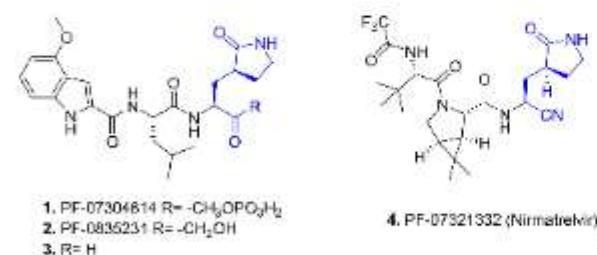
peptide bond cleavage of polyproteins.[30] The electrophilic groups of ligands which can interact with the thiol group of cysteine is commonly referred to as "warhead groups". Several short peptides and peptidomimetics featuring diverse warhead groups have been recently reported as SARS-CoV M^{pro} inhibitors. Among them, the nitrile and aldehyde warhead groups have attracted considerable attention.[31]

SARS coronavirus (CoV) 3CL protease inhibitors featuring cyclic glutamine γ-lactam ring α-nitrile motif[32] and histidine α-aldehyde motif[33] have been reported recently. We envisaged that making a hybrid analog featuring histidine α-nitrile motif would enrich the arsenal of warhead groups aimed at targeting SARS coronavirus (CoV) 3CL protease. The histidine α-nitrile motif, owing to its electrophilic character, could potentially form a covalent bond with thiol group of Cys145 unit of catalytic dyad (Cys145-His41) present in the active site of the mature dimeric M^{pro} (Figure 2, *vide supra*). The novel histidine α-nitrile motif was planned to be conjugated with various short peptide sequences of hydrophobic nature.

Inhibitor Design: The synthesis of short peptides containing the histidine α-nitrile motif is divided into two schemes (*vide infra*). The initial goal was to synthesize trityl-protected histidine aminonitrile 4 – a common intermediate for compounds 6 a–i. The intermediate 4[28] was synthesized by using solution-phase peptide coupling reaction of Fmoc-His-(Trt) OH with ammonium bicarbonate in the presence of coupling reagent HBTU/HOBt and DIPEA in DMF to obtain the amide 2 in good yield. The preparation of Fmoc-His-(Trt)-α-nitrile 3 from amide 2 was achieved by its dehydration using *in-situ* generated Vilsmeier-Haack reagent. Fmoc deprotection of 3 was achieved by a 50% mixture of *tert*-butylamine in dichloromethane to obtain the intermediate 4 in good yield (Scheme 1). Scheme 2 (*vide infra*) illustrates the coupling reaction of intermediate 4 with different carboxylic acids in the presence of HBTU/HOBt and DIPEA in DMF to furnish trityl-protected dipeptides 5 a–i, which upon removal of the trityl-protecting group with 60% TFA in DCM afforded 6 a–i in good yields.

Structure-activity relationship of histidine α-nitrile dipeptides 6 a–i: Preliminary screening was performed using infected Vero (African green monkey kidney cells, Vero (ATCC® CCL-81™)
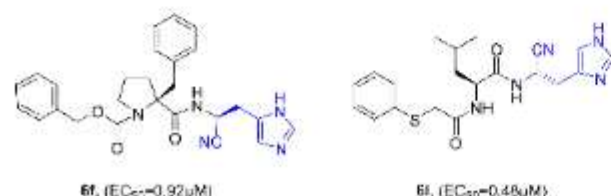

Figure 1. Structures of selected SARS-CoV-2 inhibitors (top) and a short peptide featuring histidine α-nitrile 6 f and 6 i, are described in this work.
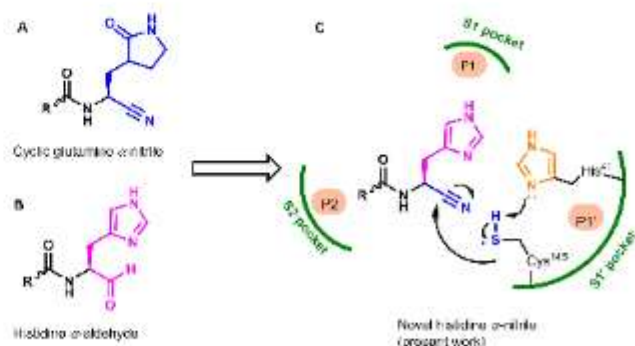

Figure 2. Illustrating the rationale behind designing histidine α-nitrile motif as SARS-CoV-2 M^{pro} inhibitor. Structural motif of glutamine γ-lactam α-nitrile (A), histidine α-aldehyde (B) and designed hybrid structure of histidine α-nitrile motif (C, present work) and its anticipated interaction in binding pockets in the active site of catalytic Cys145-His41 dyad M^{pro}.
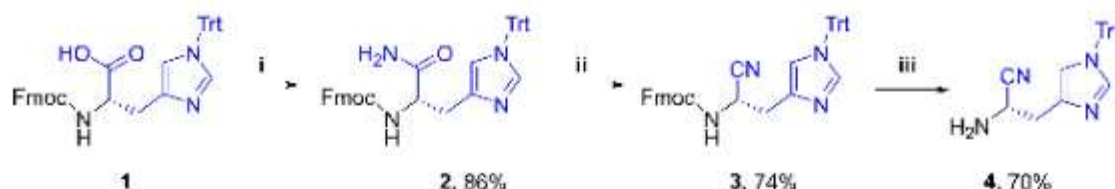
Scheme 1. Synthesis of trityl-protected histidine aminonitrile **4**. Reaction conditions: (i) Ammonium bicarbonate, HBTU, HOBt, DIPEA, dry DMF, 0 °C – rt, 10 h; (ii) (COCl)$_2$, triethylamine, dry DMF, dry ACN, 0 °C – rt, 1 h; (iii) *tert*-butylamine:DCM (1:1), rt, 30 min.
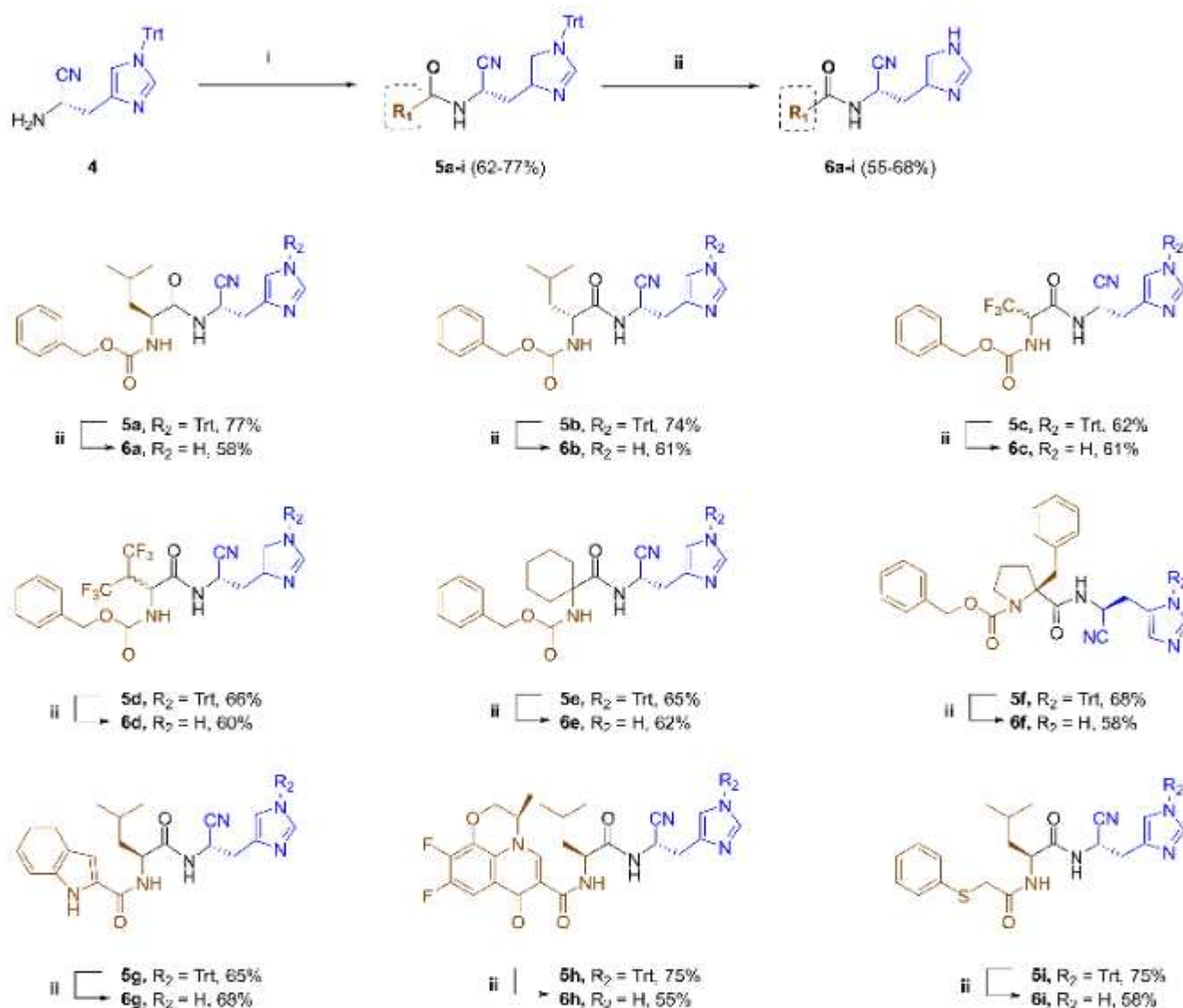
Scheme 2. Synthesis of trityl-deprotected histidine α-nitrile dipeptides **6a–i**. Reaction conditions: (i) R$_1$-COOH, HBTU, HOBt, DIPEA, DMF, 0 °C – rt, 16 h; (ii) 60% TFA in DCM, 0 °C – rt, 45 min.

cells with SARS-CoV-2 virus (A3i clade), which were treated with a series of nine compounds and RT-qPCR assays were performed to determine the percentage of viral growth reduction using different concentrations. The assay results showed that the new series of histidine α-nitrile dipeptides **6a–i** is effective for growth suppression of SARS-CoV-2 at low micro-molar concentration, except for the compounds **6a**, **6e**

and **6h** (Figure 1, *supp. info.*). We synthesized histidine α-nitrile dipeptides **6a–i** containing nitrile warhead with variable Leucine and Cbz group's substitutions. The dipeptide **6a** showed no considerable viral reduction (Figure 1a, *supp. info.*); thus, it can be speculated to serve as a platform for the optimized synthesis of potent molecules that bind to the M^{pro} target. Compound **6b** exhibited a stagnant profile of a 45%–

48% increase in viral growth suppression at concentrations between $\simeq$5 μM–25 μM (desired regime limit), which was caused by a change in the stereochemical configuration of Leucine in compound **6a**. Thus, consequent studies were conducted to modify structure **6a** to enhance its potency.

Furthermore, compound **6c** is significantly more potent than compound **6a**, as it exhibited a lead-in suppression value of 47% at 1 μM. We observed a hike in viral growth suppression with the increase in the concentration (Figure 1c, *supp. info.*), which indicates that the introduction of the trifluoro may also play a significant role in inhibition activity. The trifluoro group is partially solvent exposed, and through this interaction, it penetrates the S1 pocket with an additional hydrogen bond with Glu166 in a catalytic pocket (Figure 3a2). In **6d**, the hexafluoro-valine linked with the histidine α-nitrile motif has substantially more activity than **6a** but less in comparison to **6c**. Notably, compound **6e** from this series was inactive against SARS-CoV-2, which might be due to the presence of a cyclic system and the lack of stereochemistry in place of Leucine. Relatively, the replacement of Leucine to (S)-2-benzyl proline in compound **6f** did reveal potent behavior from the base concentration. Its activity profile is also marginally similar to compound **6c**. We understand that the presence of the 2-benzyl proline amino acid in **6f** invigorates itself to its structural counterpart **6e**. To continue our SAR studies on **6a–f** molecules, we synthesized another set of compounds that replace the Cbz-group. Previous studies indicated that the Leucine amino acid scaffolds possibly inhibited COVID virus infection in Vero cells through hydrophobic nonbonding interactions within the enzyme's catalytic pocket. We synthesized the compounds with modification on **6a**, increasing the growth suppression activity, assuming *via* the desirable protease inhibition, such as compound **6i**. Compound **6g** is structurally mimic to compound **6a** but displayed lower activity than its counterparts **6i**.

Further, by increasing the aromatic bulk, we found that the activity varied. For example, a synergistic drug-peptide conjugate, **6h**, containing a molecule of the ofloxacin drug family. When we incorporated that analogous drug entity in the place of the Cbz group, **6h** exhibited an unanticipated therapeutic profile. The compound **6i** being highly efficacious on par with **6c**, stands amidst the series of candidates, exhibiting a favorable profile of viral growth suppression (Figure 1i, *supp. info.*).

The thorough evaluation of the efficacies of our candidates of interest (COI) is defined in the results of the 'Anti-COVID activity of selected inhibitors' section. In consensus, the preliminary results concluded that 5 COIs had capable antiviral anticipations – **6c**, **6i**, **6f**, **6d** and **6g** (named in descending order of profile activity from left to right). Furthermore, the Molecular Dynamics (Figure 3), cell viability assays MTT (Figure 4) and lastly, Efficacy experiments (Figure 5) of the finalized compounds were performed to conclude their *in-vitro* anti-COVID potential. We observed that the significant COIs exhibited viral growth inhibition in the micromolar range of potency (EC_{50} from 0.5 μM–1 μM).
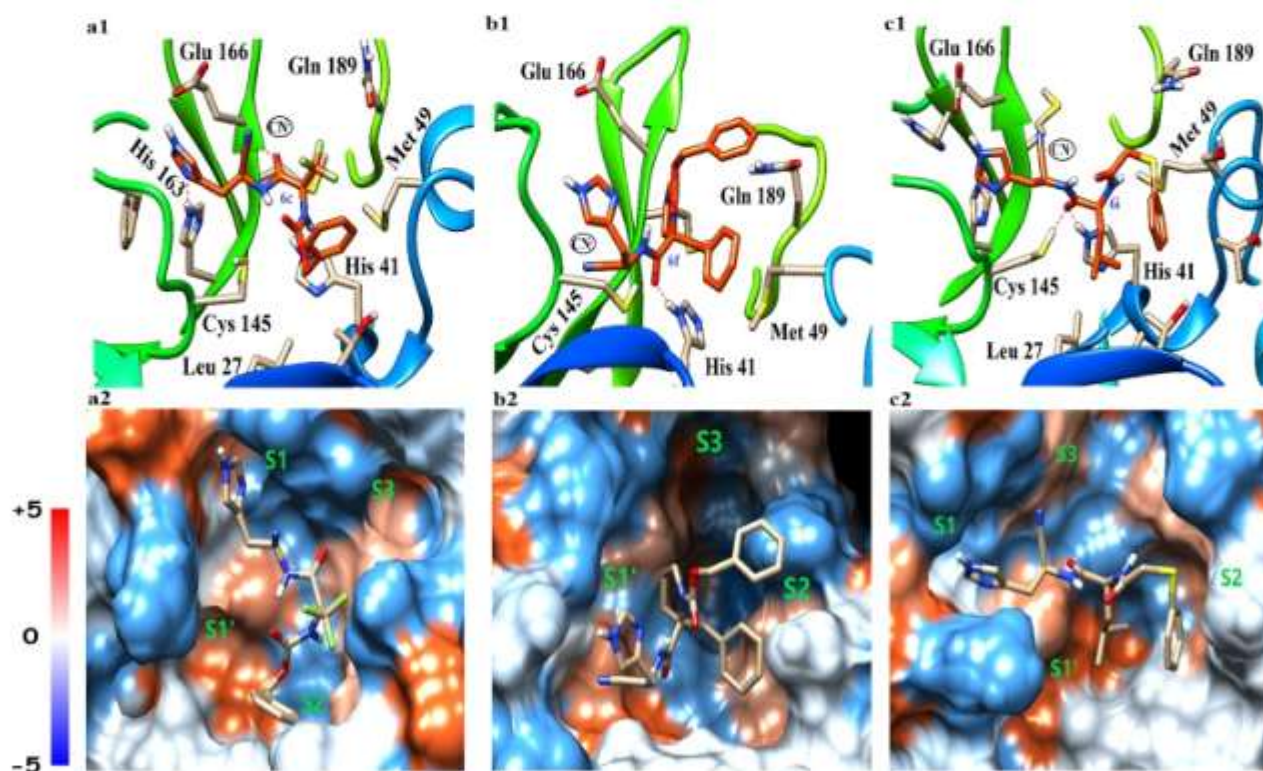

Figure 3. Binding modes of M^{pro}-inhibitor complex: Electrostatic potential surface and non-covalent interactions of the Main protease (SARS-CoV-2) with **6c** (a1 and a2), **6f** (b1 and b2) and **6i** (c1 and c2) inhibitors. Surface assigned according to Kyle-Doolittle Scale with positive values depicting hydrophobic nature.[55]
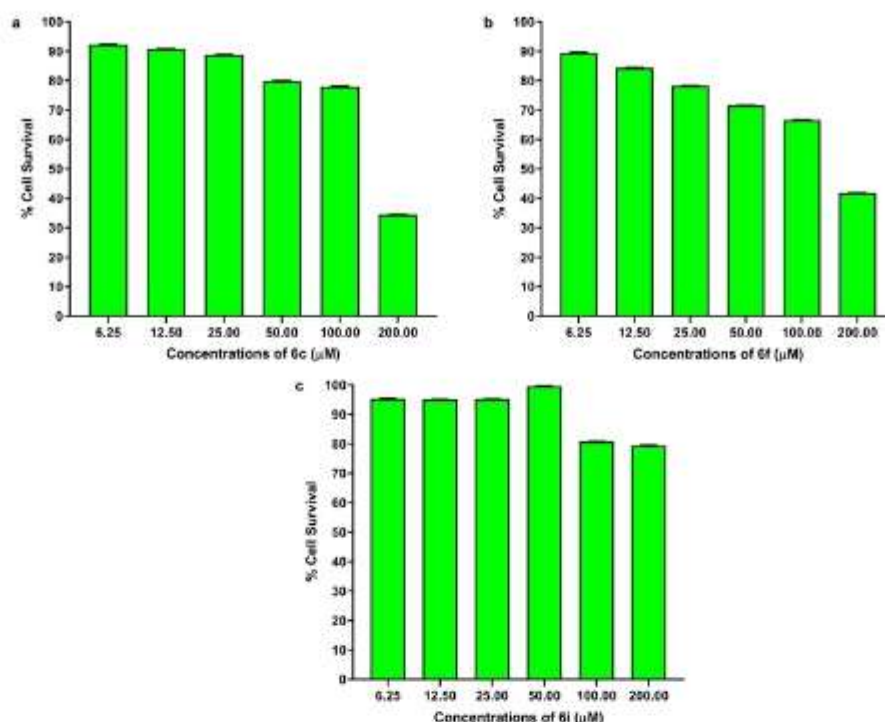
Figure 4. Cell Cytotoxicity of the inhibitor molecule (**6c**, **6f** and **6i**): Vero cells were treated with different concentrations (6.25, 12.5, 25, 50, 100 and 200 μM) of inhibitor molecules. Figure a, b and c represent the percentage of cell viability against concentrations of **6c**, **6f** and **6i** respectively. The data was analyzed using GraphPad Prism, version 8.4.2 (n = 4).
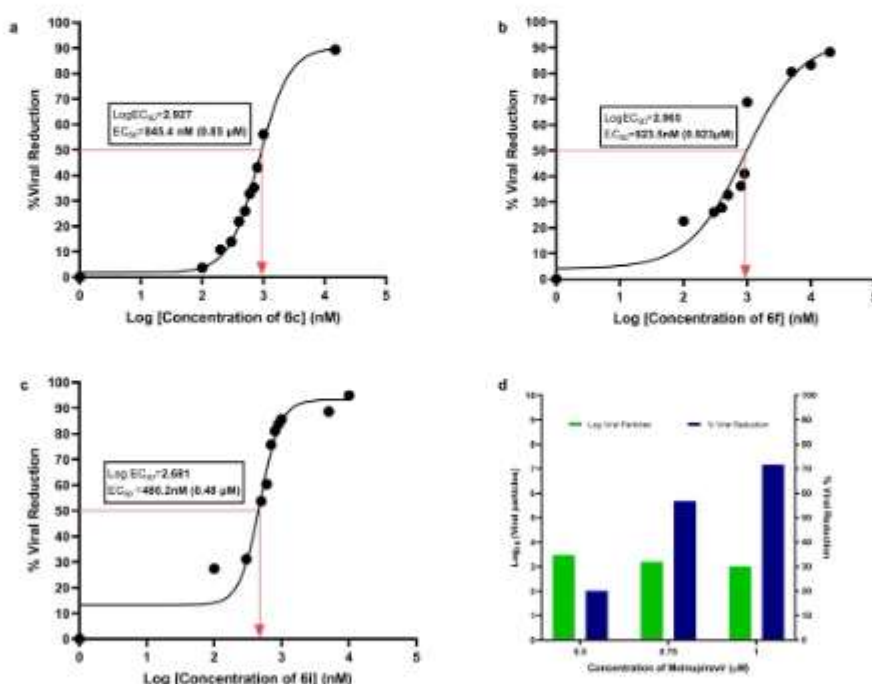

Figure 5. Anti-COVID activity of inhibitor molecules (**6c**, **6f** and **6i**): The graph represents the percentage of viral reduction *vs* different concentrations (0.1, 0.2, 0.3, 0.4, 0.5, 0.6, 0.7, 0.8, 0.9, 1, 5, 10, 15, 20 μM) of inhibitor molecules. The viral particles were enumerated by considering SARS-CoV-2 N-gene amplification using RT-qPCR. Figure 5a represents the Log EC_{50} of inhibitor (**6c**) as 2.927, which corresponds to 0.85 μM. Figure 5b represents the Log EC_{50} of inhibitor (**6f**) as 2.965 which corresponds to 0.92 μM, figure 5c the Log EC_{50} of inhibitor (**6i**) as 2.681 which corresponds to 0.48 μM and figure 5d represent the percentage of viral reduction treated with different concentration of Molnupiravir (0.5 μM, 0.75 μM and 1 μM) (n = 6).

Development of SARS-CoV-2inhibitors based on RT-qPCR assay

Cytotoxicity Assay: The results obtained from the MTT assay showed that the candidate molecules **6c** (Figure 4a), **6f** (Figure 4b) and **6i** (Figure 4c) did not elicit cytotoxicity and the cell viability ranged ~80 to 90% until 25 μM concentration suggesting that the CC_{50} value is more than 25 μM.

Anti-COVID activity of selected inhibitors (6c, 6f and 6i): The candidate inhibitor molecules showed a considerable reduction in the viral load evidenced through RT-qPCR using SARS-CoV-2 specific primers. The viral particles were enumerated and the Effective Concentration-50 (EC_{50}) for the inhibitors was calculated through 'Dose-response-Stimulation' analysis.

The inhibitor molecule, **6c** exhibited 3.7%, 10.7%, 13.9%, 21.9%, 25.9%, 32.8%, 35.1%, 43.0%, 56.0%, and 89.3% viral reduction at 0.1 μM, 0.2 μM, 0.3 μM, 0.4 μM, 0.5 μM, 0.6 μM, 0.7 μM, 0.8 μM, 1 μM and 15 μM concentrations, respectively, with one Log reduction in the viral load. The Log EC_{50} value of **6c** (2.924) corresponds to 0.85 μM (Figure 5a).

The inhibitor molecule, **6f** exhibited viral reduction of 22.5%, 26.0%, 27.7%, 32.7%, 36.1%, 41.0%, 68.7%, 80.4%, 83.2%, and 88.2% at 0.1 μM, 0.3 μM, 0.4 μM, 0.5 μM, 0.8 μM, 0.9 μM, 1 μM, 5 μM, 10 μM and 20 μM concentrations, respectively, with one Log reduction in the viral load. The Log EC_{50} value of **6f** (2.965) corresponds to 0.923 μM (Figure 5b).

The inhibitor molecule, **6i** exhibited viral reduction of 27.3%, 31.0%, 53.7%, 60.3%, 75.6%, 81.1%, 83.7%, 85.6%, 88.6%, 94.9% at 0.1 μM, 0.3 μM, 0.5 μM, 0.6 μM, 0.7 μM, 0.8 μM, 0.9 μM, 1 μM, 5 μM and 10 μM concentrations, respectively, with one Log reduction in the viral load. The Log EC_{50} value of **6i** (2.681) corresponds to 0.48 μM (Figure 5c). The antiviral drug Molnupiravir was used as an assay control drug (Figure 5d).[34]

M^{pro}-inhibitors binding interactions: Based on their bioactivity profiles, interactions of three most potent inhibitors (**6c**, **6f** and **6i**) with M^{pro} are investigated by combining molecular docking and molecular dynamics (MD) simulations (Table 1). The binding cavity of M^{pro} includes four sites namely S1, S1', S2 and S3 for these inhibitors. The MD equilibrated structure of the **6c**-M^{pro} complex shows that the binding of **6c** encompasses the S1 and S2 binding sites (Figure 3a1). In this binding mode, the imidazole group containing moiety of **6c** is stabilized by a hydrogen bond with His163 in the S1 site, while its phenyl group is located in the S2 site adjacent to Met49 (Figure 3a2). The amide group of this inhibitor forms a hydrogen bond with the backbone of Glu166 in the S1 pocket and the remaining trifluro substituent is partially solvent-exposed. Due to these interactions, **6c** penetrates deeply into the S1 region of M^{pro}. It can potentially form another hydrogen bond with the adjacent Glu166, upon the covalent binding of the nitrile warhead of **6c** to Cys145. The binding energy of **6c** computed using the Molecular Mechanics-Poisson Boltzmann Surface Area (MM-PBSA) method is −28.7 ± 5.1 Kcal/mol.

On the other hand, the **6f** inhibitor predominantly binds through hydrophobic interactions in the S1' and S2 binding sites of M^{pro} (Figure 3b1). In particular, its phenyl groups effectively occupy the S2 hydrophobic pocket surrounded by Met49 and His41 (Figure 3b2). In this mode, the sterically hindered azolidine ring is buried into the S3 site (Figure 3b1). It is further stabilized by the formation of a hydrogen bond with His41 located at the intersection of the S1' and S2 binding sites. These interactions position the nitrile warhead of **6f** close to Cys145. The binding energy of −34.9 ± 2.7 Kcal/mol for this inhibitor is approximately 6.0 Kcal/mol higher than the one computed for **6c**.

The **6i** inhibitor binds in the S1, S1', S2 binding sites of M^{pro} (Figure 3c1). Its imidazole group is positioned in the S1 site, while the Cbz group is positioned in the S2 binding site (Figure 3c1). In contrast to **6c** and **6f**, it interacts with the binding cavity predominantly through hydrogen bonding. For instance, it forms a hydrogen bond with Cys145 and His41 in the S1' site (Figure 3c2). Additionally, the β-imidazole group forms a hydrogen bond with the previously inaccessible side chain of Glu166 and positions itself in the proximity of Cys145 in the S1' binding site. Furthermore, the tertiary butyl group of the **6i** inhibitor is found to access the Thr25-Leu27 segment of the S1' binding site. The binding energy of −34.2 ± 7.1 Kcal/mol for **6i** is comparable to the calculated binding free energy for **6f** (Table 1). The inhibitor **6i** was also docked to another crystal structure (PDB ID: 6LU7). It binds in the same region of the protein with a high docking score of −13.9 (see supporting information, S50, Figure 2). It is noteworthy that these binding modes are similar to the ones proposed in a previous study using a different peptidomimetic inhibitor.[30] These results suggest that the imidazole group of histidine α-nitrile motifs preferably binds in the S1 pocket, while the Cbz terminal is in the S2. The central fragment usually occupies either the S1' binding site or is exposed to solvent. Although all of them bind in distinct modes to M^{pro} they position the critical nitrile warhead in the vicinity of Cys145.

Table 1. *In-vitro* and *in-silico* screening of potent histidine α-nitrile dipeptides.

Compound	In-vitro		In-silico		
	Cell cytotoxicity CC_{50} (μM)	Effective concentration EC_{50} (μM)	Docking score (Kcal/mol)	Binding energy (Kcal/mol)	M^{pro} pocket occupation in MD equilibrated structures
6c	>25	0.85	−10.663	−28.7 ± 5.1	S1 and S2
6f	>25	0.92	−13.447	−34.9 ± 2.7	S1'–S3
6i	>25	0.48	−13.924	−34.2 ± 7.1	S1–S2

Conclusions

The contagious epidemic threat of COVID-19 disease, caused by the SARS-CoV-2 virus and its mutated variants, wreaked havoc globally, challenging the vaccine's potential efficacy. One of the strategies to combat the pandemic is to develop a potent antiviral agent that inhibits the replication pathway of the SARS-CoV-2 virus. The M^{pro} is a fundamental enzyme for viral protein synthesis, which is required for viral replication and maturation. The development of potent M^{pro} inhibitors is thus one of the key strategies to develop potent drug molecules to fight the dreaded SARS-CoV-2. This study describes the design and synthesis of histidine α-nitrile motif embedded in a simple dipeptide backbone and the inhibitory activity of these compounds against the SARS-CoV-2 M^{pro}. The in-vitro testing of the selected inhibitors (6c, 6f and 6i) with histidine α-nitrile motif showed potential anti SARS-CoV-2 activity. In-silico studies suggest that the nitrile group of the histidine α-nitrile motif can interact with the nucleophilic thiol group of Cys145 residue of the protease, resulting in the formation of a reversible covalent thioimidate adduct in the active catalytic site of the S1' pocket. They may lead to the design of the next generation of molecules for the therapeutic prevention of SARS-CoV-2. Overall, our findings suggest that structurally modest short peptides featuring histidine α-nitrile motifs may offer utility in the development of effective therapeutics as M^{pro} inhibitors.

Experimental Section

All reagents were purchased from the highest commercial quality suppliers and used without further purifications unless otherwise stated. Reactions were carried out with laboratory-grade solvents. The purity of intermediates and final compounds were examined on pre-coated silica gel C254 TLC (Merck). All synthesized compounds were purified on silica gel (SiO$_2$) or neutral aluminum oxide (Al$_2$O$_3$). Melting points were recorded by MEL-TEMP and all melting points are uncorrected. ^{1}H, ^{13}C{^{1}H} and DEPT-135 spectra were recorded on Bruker AV-400 and AV-500 MHz using DMSO-d_6/CD$_3$OD as solvents and TMS as internal standard. ^{1}H and ^{13}C {^{1}H} NMR chemical shifts are expressed in parts per million (ppm, δ scale) and were referenced to NMR solvent DMSO-d_6 δ 2.50, 39.8 ppm and CD$_3$OD δ 4.87, 3.31, 49.15 ppm, respectively. The following abbreviations were used to describe peak patterns when appropriate; br. s. = broad singlet, s = singlet, d = doublet, t = triplet, q = quartet, m = multiplet, and coupling constant (J). High-resolution mass spectra (HRMS) were recorded on Agilent LC-TOF mass spectrometer by electrospray ionization-time off-flight reflection (ESI-TOF) experiments.

(9H-fluoren-9-yl)methyl(S)-(1-amino-1-oxo-3-(1-trityl-1H-imidazol-4-yl)propan-2-yl)carbamate (2). A solution containing Fmoc-His-(Trt)-OH (2 g, 3.2 mmol) in dry DMF (10 ml) was cooled at 0 °C. To this reaction mixture, HBTU (1.84 g, 4.84 mmol) was added, followed by the addition of HOBt (0.436 g, 3.23 mmol), DIPEA (1.69 ml, 9.68 mmol) and ammonium bicarbonate (0.510 g, 6.4 mmol). The reaction mixture was stirred at 0 °C for 10 minutes and then at room temperature for 10 h. After completion of the reaction, the reaction mixture was added to ice water and extracted with EtOAc twice. The combined EtOAc layer was washed sequentially with sat. NaHCO$_3$, sat. KHSO$_4$ and brine solution. The organic layer was then dried over Na$_2$SO$_4$, filtered and concentrated

under vacuum. Purification by column chromatography on neutral alumina (eluent: 5% MeOH:DCM, R$_f$ = 0.4) afforded compound 2 (1.7 g, 86%) as an amorphous pale white solid. [α]$^{28}_D$: −12.64 (c = 0.52, CHCl$_3$); mp: 100–105 °C; ^{1}H-NMR (400 MHz, DMSO-d_6) δ 7.86 (m, 2H), 7.67 (t, J = 7.7 Hz, 2H), 7.47-7.16 (m, 17H), 7.03 (d, J = 7.6 Hz, 6H), 6.69 (s, 1H), 4.27–4.06 (m, 4H), 2.79 (m, 2H); ^{13}C{^{1}H} NMR (100 MHz, DMSO-d_6) δ 173.4, 155.8, 143.9, 143.8, 142.3, 140.7, 140.7, 137.5, 137.2, 129.3, 129.3, 129.3, 129.3, 129.3, 129.3, 129.3, 129.0, 128.2, 128.2, 128.2, 128.2, 128.2, 128.1, 128.0, 127.7, 127.7, 127.7, 127.1, 125.4, 125.3, 121.4, 120.1, 120.1, 118.9, 109.8, 74.4, 65.7, 54.6, 46.7, 31.0; HRMS (ESI-TOF) m/z [M+H]$^{+}$ calcd for C$_{40}$H$_{35}$N$_4$O$_3$: 619.2704, found 619.2703 [M+H]$^{+}$. Note: The residual solvent peak appear at. δ 1.91.

(9H-fluoren-9-yl)methyl(S)-(1-cyano-2-(1-trityl-1H-imidazol-4-yl)ethyl)carbamate (3). Dry DMF (1.25 mL, 16.2 mmol) and oxalyl chloride (0.97 mL, 11.3 mmol) were taken in dry acetonitrile (10 mL) maintained at 0 °C under argon atmosphere. The reaction mixture was stirred for 15 min at 0 °C, when a white precipitate was formed. Then triethylamine (1.12 mL, 8.1 mmol) was added followed by the addition of amide 2 (1 g, 1.6 mmol) and the reaction mixture was stirred at room temperature until the starting material amide 2 disappeared (~1 h). The reaction mixture was then neutralized by the addition of triethylamine (1.12 mL, 8.1 mmol). Ice cold water was added to the reaction mixture followed by extraction with dichloromethane. Organic layer was then dried over Na$_2$SO$_4$ and was evaporated under vacuum. Purification by column chromatography on neutral alumina (eluent: 50% EtOAc:Pet ether, R$_f$ 0.8) afforded compound 3 (0.72 g, 74%) as an off-white solid. [α]$^{28}_D$: −10.38 (c = 0.41, CHCl$_3$); mp: 95–100 °C; ^{1}H-NMR (500 MHz, DMSO-d_6) δ 8.25 (d, J = 8.0 Hz, 1H), 7.89 (d, J = 7.4 Hz, 2H), 7.66 (d, J = 7.4 Hz, 2H), 7.45–7.25 (m, 14H), 7.11–6.99 (m, 6H), 6.84 (s, 1H), 4.77 (q, J = 7.8 Hz, 1H), 4.38 (d, J = 6.7 Hz, 2H), 4.21 (t, J = 6.5 Hz, 1H), 2.96 (m, 2H); ^{13}C{^{1}H} NMR (125 MHz, DMSO-d_6) δ 155.4, 143.7, 143.6, 140.8, 140.8, 138.1, 135.0, 129.2, 129.2, 129.2, 129.2, 129.2, 129.2, 129.2, 128.9, 128.9, 128.9, 128.9, 128.9, 128.2, 128.0, 127.7, 127.7, 127.7, 127.1, 125.1, 125.0, 121.4, 120.2, 120.0, 119.9, 119.3, 109.8, 74.6, 66.0, 46.6, 42.9, 31.0; HRMS (ESI-TOF) m/z [M+H]$^{+}$ calcd for C$_{40}$H$_{33}$N$_4$O$_2$: 601.2598, found 601.2607 [M+H]$^{+}$. Note: The residual solvent peak appear at. δ 1.91, 1.24.

(S)-2-amino-3-(1-trityl-1H-imidazol-4-yl) propanenitrile (4). Compound 3 (1.7 g, 2.83 mmol) was stirred in tert-butylamine:DCM (1:1) solution for 30 min. at 0 °C. After completion of Fmoc deprotection, as judged by TLC, the reaction mixture was stripped off solvents and washed with pet ether for 2–3 times to remove residual tert-butylamine and Fmoc deprotection side products. The resulting solid was filtered and dried under vacuum affording 4 (0.75 g, 70%) as a pale white solid. [α]$^{28}_D$: −6.36 (c = 0.16, CHCl$_3$); mp: 130–135 °C; ^{1}H-NMR (400 MHz, DMSO-d_6) δ 7.41–7.35 (m, 10H), 7.30 (d, J = 1.1 Hz, 1H), 7.08 (m, 6H), 6.78 (s, 1H), 3.96 (t, J = 7.2 Hz, 1H), 2.78 (d, J = 7.7 Hz, 2H); ^{13}C{^{1}H} NMR (100 MHz, DMSO-d_6) δ 142.3, 142.3, 142.3, 138.1, 136.4, 129.4, 129.4, 129.4, 129.4, 129.4, 129.4, 129.4, 129.4, 128.4, 128.4, 128.4, 128.4, 128.4, 128.4, 128.2, 122.8, 119.8, 74.7, 44.0, 33.9; HRMS (ESI-TOF) m/z [M+H]$^{+}$ calcd for C$_{25}$H$_{22}$N$_4$: 379.1917, found 379.1912 [M+H]$^{+}$ and 401.1730 [M+Na]$^{+}$.

Benzyl((S)-1-(((S)-1-cyano-2-(1-trityl-1H-imidazol-4-yl)ethyl)amino)-4-methyl-1-oxopentan-2-yl)carbamate (5a). A solution containing Cbz-^{L}Leu-OH (0.10 g, 0.38 mmol) in dry DMF (2 ml) was cooled at 0 °C. To the reaction mixture, HBTU (0.21 g, 0.57 mmol) was added followed by the addition of HOBt (0.05 g, 0.38 mmol), DIPEA (0.19 mL, 1.13 mmol) and amine 4 (0.17 g, 0.45 mmol). The reaction mixture was stirred at 0 °C for 10 minutes and then at room temperature for 10 h. After completion of the reaction, the reaction mixture was poured into ice water and extracted with EtOAc twice. The combined EtOAc layer was washed

sequentially with sat. KHSO$_4$, sat. NaHCO$_3$ and brine solution. EtOAc layer was then dried over Na$_2$SO$_4$, filtered and concentrated under vacuum. Purification by column chromatography on neutral alumina (eluent: 50% EtOAc:Pet ether, R$_f$ 0.5) afforded compound **5a** (0.182 g, 77%) as a white solid. $[\alpha]^{25}_D$: −12.02 (c = 0.13, CHCl$_3$); mp: 60–70 °C; ^{1}H-NMR (400 MHz, DMSO-d_6) δ 8.87 (d, J = 7.5 Hz, 1H), 7.54 (d, J = 8.1 Hz, 1H), 7.46–7.15 (m, 15H), 7.12–7.03 (m, 6H), 6.88 (s, 1H), 5.05–4.82 (m, 3H), 4.04 (m, 1H), 2.96 (m, 2H), 1.60 (m, 1H), 1.53–1.43 (m, 1H), 1.38 (m, 1H), 0.91–0.79 (m, 6H); ^{13}C{^{1}H} NMR (100 MHz, DMSO-d_6) δ 172.5, 156.0, 142.2, 142.2, 142.2, 138.1, 136.9, 135.1, 129.3, 129.3, 129.3, 129.3, 129.3, 129.3, 129.3, 129.3, 128.3, 128.2, 128.2, 128.2, 128.2, 128.0, 128.0, 128.0, 127.7, 127.6, 127.6, 119.9, 119.0, 74.6, 65.4, 52.9, 40.8, 40.3, 39.5, 30.5, 24.2, 22.9, 21.3; HRMS (ESI-TOF) m/z [M+H]$^+$ calcd for C$_{39}$H$_{40}$N$_5$O$_3$: 626.3126, found 626.3113 [M+H]$^+$.

Benzyl ((S)-1-(((S)-1-cyano-2-(1H-imidazol-4-yl)ethyl)amino)-4-methyl-1-oxopentan-2-yl)carbamate (6a). The trityl protected dipeptide **5a** (0.07 g) was dissolved in 60% solution of TFA in DCM at 0 °C and stirred for 45 minutes. After completion of trityl deprotection, as judged by TLC, the reaction mixture was stripped off solvents and washed with diethyl ether to remove residual TFA and trityl deprotection side products. The TFA salt was neutralized with NaHCO$_3$ and then extracted with 1:2 mixtures of MeOH and EtOAc and organic layer was dried over Na$_2$SO$_4$ and evaporated under vacuum to afford compound **6a** (0.025 g, 58%) as a white solid. $[\alpha]^{25}_D$: −15.75 (c = 0.18, MeOH); mp: 55–60 °C; ^{1}H-NMR (400 MHz, CD$_3$OD) δ 8.19$_{rotamer}$ (s, 1H), 7.30–7.15$_{rotamer}$ (m, 5H), 7.04$_{rotamer}$ (d, J = 22.8 Hz, 1H), 5.06–4.91$_{rotamer}$ (m, 2H), 4.66–4.53$_{rotamer}$ (m, 1H), 4.04–3.86$_{rotamer}$ (m, 1H), 3.17–2.79$_{rotamer}$ (m, 2H), 1.57–1.48$_{rotamer}$ (m, 1H), 1.45–1.30$_{rotamer}$ (m, 2H), 0.83–0.74$_{rotamer}$ (m, 6H); ^{13}C{^{1}H} NMR (100 MHz, CD$_3$OD) δ 175.5, 174.8, 138.1, 138.1, 130.9, 129.5, 129.5, 129.0, 128.8, 128.8, 118.5, 116.8, 67.8, 55.3, 53.5, 41.6, 28.7, 25.8, 23.3, 21.9; HRMS (ESI-TOF) m/z [M+H]$^+$ calcd for C$_{20}$H$_{26}$N$_5$O$_3$: 384.2030, found 384.2027 [M+H]$^+$. *Note:* The residual solvent peak appear at. δ 5.39, 1.13. Rotamer formation has been noted in related derivatives.[36]

Benzyl((R)-1-(((S)-1-cyano-2-(1-trityl-1H-imidazol-4-yl)ethyl)amino)-4-methyl-1-oxopentan-2-yl)carbamate (5b). The synthetic method of **5a** was adopted to synthesize **5b**; white solid (0.175 g, 74%). $[\alpha]^{25}_D$: −4.95 (c = 0.18, CHCl$_3$); mp: 65–70 °C; ^{1}H-NMR (400 MHz, DMSO-d_6) δ 8.91 (s, 1H), 7.54 (d, J = 7.8 Hz, 1H), 7.32 (m, 15H), 7.08 (s, 6H), 6.86 (s, 1H), 5.10–4.88 (m, 3H), 4.02 (d, J = 1.3 Hz, 1H), 2.94 (m, 2H), 1.58 (m, 1H), 1.48–1.38 (m, 1H), 1.29 (m, 1H), 0.82 (d, J = 15.1 Hz, 6H); ^{13}C{^{1}H} NMR (100 MHz, DMSO-d_6) δ 172.4, 156.0, 142.2, 142.2, 142.2, 138.1, 136.9, 135.1, 129.3, 129.3, 129.3, 129.3, 129.3, 129.3, 129.3, 128.3, 128.2, 128.2, 128.2, 128.2, 128.1, 128.1, 128.1, 127.7, 127.7, 127.7, 119.8, 119.2, 74.6, 65.5, 52.9, 40.5, 40.3, 39.5, 30.7, 24.1, 22.9, 21.2; HRMS (ESI-TOF) m/z [M+H]$^+$ calcd for C$_{39}$H$_{40}$N$_5$O$_3$: 626.3126, found 626.3114 [M+H]$^+$ and 648.2922 [M+Na]$^+$.

Benzyl((R)-1-(((S)-1-cyano-2-(1H-imidazol-4-yl)ethyl)amino)-4-methyl-1-oxopentan-2-yl)carbamate (6b). The synthetic method of **6a** was adopted to synthesize **6b**; white solid (0.141 g, 61%); mp: 60–65 °C; ^{1}H-NMR (400 MHz, CD$_3$OD) δ 8.65$_{rotamer}$ (d, J = 35.0 Hz, 1H), 7.26–7.11$_{rotamer}$ (m, 6H), 5.04–4.93$_{rotamer}$ (m, 2H), 4.68–4.58$_{rotamer}$ (m, 1H), 4.02–3.85$_{rotamer}$ (m, 1H), 3.30$_{rotamer}$ (m, 1H), 2.97$_{rotamer}$ (m, 1H), 1.60–1.32$_{rotamer}$ (m, 2H), 1.27$_{rotamer}$ (m, 1H), 0.88–0.71$_{rotamer}$ (m, 6H; ^{13}C{^{1}H} NMR (100 MHz, CD$_3$OD) δ 175.7, 174.6, 138.1, 135.0, 129.8, 129.5, 129.3, 128.7, 128.6, 127.8, 118.5, 117.1, 67.8, 55.4, 53.1, 41.3, 27.8, 25.8, 23.0, 22.2; HRMS (ESI-TOF) m/z [M+H]$^+$ calcd for C$_{20}$H$_{26}$N$_5$O$_3$: 384.2030, found 384.2026 [M+H]$^+$. *Note:* The residual solvent peak appear at. δ 3.49, 1.07. Rotamer formation has been noted in related derivatives.[36]

Benzyl(3-(((S)-1-cyano-2-(1-trityl-1H-imidazol-4-yl)ethyl)amino)-1,1,1-trifluoro-3-oxopropan-2-yl)carbamate (5c). The synthetic method of **5a** was adopted to synthesize **5c**; white solid (0.071 g, 62%); mp: 160–165 °C; ^{1}H-NMR (400 MHz, DMSO-d_6) δ 9.47 (d, J = 9.0 Hz, 1H), 8.60 (m, 1H), 7.34 (m, 15H), 7.07 (d, J = 7.6 Hz, 6H), 6.88 (d, J = 7.8 Hz, 1H), 5.04 (m, 4H), 3.06–2.81 (m, 2H); ^{13}C{^{1}H} NMR (100 MHz, DMSO-d_6) δ 163.3, 156.1, 142.2, 142.2, 142.2, 138.2, 136.4, 134.6, 129.3, 129.3, 129.3, 129.3, 129.3, 129.3, 129.3, 129.3, 128.5, 128.5, 128.3, 128.3, 128.2, 128.2, 128.1, 128.1, 127.9, 127.9, 127.6, 126.7, 120.1, 118.6, 118.4, 74.8, 66.5, 41.1, 40.8, 30.5; HRMS (ESI-TOF) m/z [M+H]$^+$ calcd for C$_{36}$H$_{31}$N$_5$O$_3$F$_3$: 638.2374, found 638.2369 [M+H]$^+$.

Benzyl(3-(((S)-1-cyano-2-(1H-imidazol-4-yl)ethyl)amino)-1,1,1-trifluoro-3-oxopropan-2-yl)carbamate (6c). The synthetic method of **6a** was adopted to synthesize **6c**; white solid (0.141 g, 61%); mp: 80–85 °C; ^{1}H-NMR (400 MHz, CD$_3$OD) δ 7.71$_{rotamer}$ (d, J = 4.9 Hz, 1H), 7.31–7.12$_{rotamer}$ (m, 5H), 6.98$_{rotamer}$ (d, J = 9.8 Hz, 1H), 5.10–4.86$_{rotamer}$ (m, 4H), 3.12–2.84$_{rotamer}$ (m, 2H); ^{13}C{^{1}H} NMR (100 MHz, CD$_3$OD) δ 175.7, 165.2, 137.7, 132.9, 129.5, 129.3, 129.2, 129.0, 128.9, 118.7, 118.2, 116.8, 68.40, 57.4, 57.0, 42.4, 31.02; HRMS (ESI-TOF) m/z [M+H]$^+$ calcd for C$_{17}$H$_{17}$N$_5$O$_3$F$_3$: 396.1278, found 396.1273 [M+H]$^+$. *Note:* The residual solvent peak appear at. δ 1.88. Rotamer formation has been noted in related derivatives.[36]

Benzyl(1-(((S)-1-cyano-2-(1-trityl-1H-imidazol-4-yl)ethyl)amino)-4,4,4-trifluoro-1-oxo-3(trifluoromethyl)butan-2-yl)carbamate (5d). The synthetic method of **5a** was adopted to synthesize **5d**; white solid (0.172 g, 66%); mp:75–80 °C; ^{1}H-NMR (400 MHz, DMSO-d_6) δ 9.23 (m, 1H), 8.08 (m, 1H), 7.46–7.23 (m, 15H), 7.13–7.03 (m, 6H), 6.89 (m, 1H), 5.20–4.94 (m, 4H), 4.60–4.42 (m, 1H), 3.10–2.90 (m, 2H); ^{13}C{^{1}H} NMR (100 MHz, DMSO-d_6) δ 167.0, 156.0, 142.1, 142.1, 142.1, 138.2, 136.5, 134.9, 129.3, 129.3, 129.3, 129.3, 129.3, 129.3, 129.3, 129.3, 128.3, 128.3, 128.3, 128.3, 128.3, 128.3, 128.2, 128.1, 127.9, 127.6, 127.5, 120.0, 119.9, 118.5, 118.3, 74.7, 66.2, 50.0, 41.6, 31.0, 22.1, 14.0; HRMS (ESI-TOF) m/z [M+H]$^+$ calcd for C$_{38}$H$_{32}$N$_5$O$_3$F$_6$: 720.2404, found 720.2390 [M+H]$^+$. *Note:* The residual solvent peak appear at. δ 1.25, 0.86.

Benzyl(1-(((S)-1-cyano-2-(1H-imidazol-4-yl)ethyl)amino)-4,4,4-trifluoro-1-oxo-3 (trifluorom thyl)butan-2-yl)carbamate (6d). The synthetic method of **6a** was adopted to synthesize **6d**; white solid (0.12 g, 60%); mp: 65–70 °C; ^{1}H-NMR (400 MHz, CD$_3$OD) δ 8.82$_{rotamer}$ (m, 1H), 7.48–7.28$_{rotamer}$ (m, 7H), 5.31–5.07$_{rotamer}$ (m, 3H), 4.38$_{rotamer}$ (m, 1H), 3.40$_{rotamer}$ (m, 1H), 3.26–3.02$_{rotamer}$ (m, 1H).; ^{13}C{^{1}H} NMR (100 MHz, CD$_3$OD) δ 173.9, 169.6, 137.7, 135.6, 134.9, 129.8, 129.5, 129.2, 129.0, 128.9, 128.8, 119.4, 118.5, 118.0, 68.5, 53.5, 41.4, 28.0, 14.4; HRMS (ESI-TOF) m/z [M+H]$^+$ calcd for C$_{19}$H$_{18}$F$_6$N$_5$O$_3$: 478.1308, found 478.1299 [M+H]$^+$. *Note:* The residual solvent peak appear at. δ 1.30, 1.19, 0.91. Rotamer formation has been noted in related derivatives.[36]

Benzyl(1-((1-cyano-2-(1-trityl-1H-imidazol-4-yl)ethyl)carbamoyl)cyclohexyl)carbamate (5e). The synthetic method of **5a** was adopted to synthesize **5e**; white solid (0.225 g, 65%); $[\alpha]^{25}_D$: 0.75 (c = 0.16, CHCl$_3$); mp: 80–85 °C; ^{1}H-NMR (400 MHz, DMSO-d_6) δ 8.52 (d, J = 7.7 Hz, 1H), 7.47–7.32 (m, 10H), 7.28 (m, 6H), 7.13–7.00 (m, 6H), 6.84 (s, 1H), 5.05–4.78 (m, 3H), 2.90 (d, J = 6.5 Hz, 2H), 1.88 (d, J = 11.4 Hz, 2H), 1.65–1.57 (m, 2H), 1.44 (s, 4H), 1.29–1.15 (m, 2H); ^{13}C{^{1}H} NMR (100 MHz, DMSO-d_6) δ 174.4, 154.7, 142.1, 142.1, 142.1, 138.1, 137.0, 135.5, 129.3, 129.3, 129.3, 129.3, 129.3, 129.3, 129.3, 129.3, 128.2, 128.2, 128.2, 128.2, 128.2, 128.2, 128.1, 128.1, 127.7, 127.7, 127.5, 119.8, 119.1, 74.6, 65.1, 58.8, 40.8, 30.7, 30.4, 30.1, 30.3, 24.9, 20.9, 20.9; HRMS (ESI-TOF) m/z [M+H]$^+$ calcd for C$_{40}$H$_{40}$N$_5$O$_3$: 638.3126, found 638.3114 [M+H]$^+$. *Note:* The residual solvent peak appear at. δ 0.85.

Benzyl(S)-(1-((1-cyano-2-(1H-imidazol-4-yl)ethyl)carbamoyl)cyclohexyl)carbamate (6e). The synthetic method of 6a was adopted to synthesize 6e; white solid (0.069 g, 62%); $[\alpha]^{25}_D$: −28.81 (c=0.1, MeOH); mp: 115–120 °C; ^{1}H-NMR (500 MHz, CD$_3$OD) δ 7.46$_{rotamer}$ (s, 1H), 7.28–7.10$_{rotamer}$ (m, 5H), 6.76$_{rotamer}$ (s, 1H), 4.99–4.90$_{rotamer}$ (m, 2H), 4.46$_{rotamer}$ (m, 1H), 3.10–2.84$_{rotamer}$ (m, 2H), 1.87–1.63$_{rotamer}$ (m, 2H), 1.57–1.09$_{rotamer}$ (m, 8H); ^{13}C{^{1}H}NMR (125 MHz, CD$_3$OD) δ 177.4, 157.8, 138.0, 136.4, 129.5, 129.1, 128.9, 128.6, 127.9, 118.5, 79.8, 67.7, 60.7, 54.5, 49.8, 34.2, 32.0, 30.7, 29.1, 26.3, 22.3; HRMS (ESI-TOF) m/z [M+H]$^+$ calcd for C$_{21}$H$_{26}$N$_5$O$_3$: 396.2030, found 396.2027 [M+H]$^+$. *Note:* The residual solvent peak appear at. δ 0.78. Rotamer formation has been noted in related derivatives.[36]

Benzyl (S)-2-benzyl-2-(2-(((S)-1-cyano-2-(1-trityl-1H-imidazol-4-yl)ethyl)amino)-2-oxoethyl) pyrrolidine-1-carboxylate (5f). The synthetic method of 5a was adopted to synthesize 5f; white solid (0.121 g, 68%); $[\alpha]^{25}_D$: −10.88 (c=0.10, CHCl$_3$); mp: 65–70 °C; ^{1}H-NMR (400 MHz, DMSO-d_6) δ 8.68$_{rotamer}$ (m, 1H), 7.44–7.34$_{rotamer}$ (m, 15H), 7.21$_{rotamer}$ (m, 4H), 7.12–7.05$_{rotamer}$ (m, 6H), 6.99$_{rotamer}$ (t, J=6.2 Hz, 2H), 6.92$_{rotamer}$ (s, 1H), 5.18$_{rotamer}$ (m, 1H), 5.05–4.96$_{rotamer}$ (m, 2H), 3.49$_{rotamer}$ (m, 2H), 3.16$_{rotamer}$ (m, 1H), 3.05$_{rotamer}$ (t, J=12.3 Hz, 1H), 2.95$_{rotamer}$ (d, J=6.9 Hz, 1H), 2.83–2.70$_{rotamer}$ (m, 1H), 2.20$_{rotamer}$ (t, J=7.3 Hz, 1H), 2.10–1.96$_{rotamer}$ (m, 1H), 1.92–1.79$_{rotamer}$ (m, 1H), 1.50–1.37$_{rotamer}$ (m, 1H); ^{13}C{^{1}H}NMR (100 MHz, DMSO-d_6) δ 173.4, 153.4, 142.1, 142.1, 142.1, 138.1, 137.1, 136.8, 135.3, 130.4, 130.4, 129.3, 129.3, 129.3, 129.3, 129.3, 129.3, 129.3, 128.3, 128.3, 128.3, 128.3, 128.2, 128.2, 128.1, 127.9, 127.8, 127.6, 126.5, 125.7, 119.9, 119.7, 119.0, 79.2, 74.7, 69.2, 68.5, 65.9, 47.9, 41.1, 36.5, 35.2, 21.9, 21.9; HRMS (ESI-TOF) m/z [M+H]$^+$ calcd for C$_{45}$H$_{47}$N$_5$O$_3$: 700.3282, found 700.3271 [M+H]$^+$. *Note:* The residual solvent peak appear at. δ 5.73, 1.22, 0.84. Rotamer formation has been noted in related derivatives.[37]

Benzyl(S)-2-benzyl-2-(((S)-1-cyano-2-(1H-imidazol-4-yl)ethyl)carbamoyl)pyrrolidine-1-carboxylate (6f). The synthetic method of 6a was adopted to synthesize 6f; white solid (0.057 g, 58%); $[\alpha]^{25}_D$: −60.50 (c=0.10, MeOH); mp: 95–100 °C; 1H-NMR (400 MHz, CD$_3$OD) δ 7.38–7.20$_{rotamer}$ (m, 5H), 7.18–6.98$_{rotamer}$ (m, 4H), 6.91–6.76$_{rotamer}$ (m, 3H), 5.24$_{rotamer}$ (m, 1H), 4.96$_{rotamer}$ (m, 1H), 4.58$_{rotamer}$ (m, 1H), 4.43$_{rotamer}$ (m, 1H), 3.61–3.37$_{rotamer}$ (m, 2H), 3.02$_{rotamer}$ (m, 3H), 2.65$_{rotamer}$ (m, 1H), 2.16–1.94$_{rotamer}$ (m, 1H), 1.42$_{rotamer}$ (m, 1H), 1.01–0.87$_{rotamer}$ (m, 1H); ^{13}C{^{1}H}NMR (100 MHz, CD$_3$OD) δ 172.4, 161.2, 142.1, 138.1, 136.5, 135.1, 131.2, 129.3, 129.3, 128.2, 128.1, 128.1, 127.0, 123.5, 121.6, 119.9, 119.8, 119.2, 112.3, 103.7, 74.7, 51.1, 40.9, 24.4, 23.0, 21.3; HRMS (ESI-TOF) m/z [M+H]$^+$ calcd for C$_{26}$H$_{28}$N$_5$O$_3$: 458.2187, found 458.2184 [M+H]$^+$. *Note:* The residual solvent peak appear at. δ 1.87. Rotamer formation has been noted in related derivatives.[36]

N-((S)-1-(((S)-1-cyano-2-(1-trityl-1H-imidazol-4-yl)ethyl)amino)-4-methyl-1-oxopentan-2-yl)-1H-indole-2-carboxamide (5g). The synthetic method of 5a was adopted to synthesize 5g; yellow solid (0.3 g, 65%); $[\alpha]^{25}_D$: −10.56 (c=0.13, CHCl$_3$); mp: 130–135 °C; ^{1}H-NMR (400 MHz, DMSO-d_6) δ 11.56 (s, 1H), 9.05 (m, 1H), 8.55 (d, J=8.1 Hz, 1H), 7.58 (m, 1H), 7.46–7.31 (m, 10H), 7.26 (m, 1H), 7.18 (m, 2H), 7.04 (m, 7H), 6.86 (s, 1H), 5.09–4.89 (m, 1H), 4.55 (m, 1H), 2.97 (m, 2H), 1.78–1.58 (m, 2H), 1.49 (m, 1H), 0.98–0.78 (m, 6H); ^{13}C{^{1}H}NMR (100 MHz, DMSO-d_6) δ 172.4, 161.2, 142.1, 142.1, 142.1, 138.1, 136.5, 135.1, 131.2, 129.3, 129.3, 129.3, 129.3, 129.3, 129.3, 129.3, 129.3, 128.2, 128.2, 128.2, 128.2, 128.2, 128.1, 128.1, 127.0, 123.5, 121.6, 119.9, 119.8, 119.2, 118.9, 112.3, 103.7, 103.6, 74.7, 51.1, 40.9, 24.4, 23.0, 21.3; HRMS (ESI-TOF) m/z [M+H]$^+$ calcd for C$_{40}$H$_{39}$N$_6$O$_2$: 635.3129, found 635.3123 [M+H]$^+$.

N-((S)-1-(((S)-1-cyano-2-(1H-imidazol-4-yl)ethyl)amino)-4-methyl-1-oxopentan-2-yl)-1H-indole-2-carboxamide (6g). The synthetic method of 6a was adopted to synthesize 6g; yellow solid (0.105 g,

68%); $[\alpha]^{25}_D$: 3.10 (c=0.25, CHCl$_3$); mp: 150–155 °C; ^{1}H-NMR (400 MHz, CD$_3$OD) δ 7.49$_{rotamer}$ (m, 1H), 7.32$_{rotamer}$ (m, 1H), 7.22–7.04$_{rotamer}$ (m, 3H), 6.96$_{rotamer}$ (m, 2H), 6.79$_{rotamer}$ (m, 1H), 4.66–4.27$_{rotamer}$ (m, 2H), 2.94$_{rotamer}$ (m, 2H), 1.72–1.37$_{rotamer}$ (m, 3H), 0.91–0.73$_{rotamer}$ (m, 6H); ^{13}C{^{1}H}NMR (100 MHz, CD$_3$OD) δ 175.0, 164.1, 138.4, 136.7, 136.2, 131.4, 128.8, 125.3, 122.9, 121.2, 118.2, 113.1, 105.5, 54.3, 41.2, 29.6, 26.1, 25.7, 23.3, 22.6, 21.9; HRMS (ESI-TOF) m/z [M+H]$^+$ calcd for C$_{21}$H$_{25}$N$_5$O$_3$: 393.2034, found 393.2018 [M+H]$^+$. *Note:* Rotamer formation has been noted in related derivatives.[36]

(R)-N-((S)-1-(((S)-1-cyano-2-(1-trityl-1H-imidazol-4-yl)ethyl)amino)-4-methyl-1-oxopentan-2-yl)-9,10-difluoro-3-methyl-7-oxo-2,3-dihydro-7H-[1,4]oxazino[2,3,4-ij]quinoline-6-carboxamide (5h). The synthetic method of 5a was adopted to synthesize 5h; pale white solid (0.144 g, 75%); $[\alpha]^{25}_D$: −12.02 (c=0.11, CHCl$_3$); mp: 125–130 °C; ^{1}H-NMR (400 MHz, DMSO-d_6) δ 10.30–10.12 (m, 1H), 9.07 (m, 1H), 8.89–8.73 (m, 1H), 7.61 (m, 1H), 7.44–7.32 (m, 9H), 7.22 (m, 1H), 7.05 (d, J=6.3 Hz, 6H), 6.86 (s, 1H), 4.97 (m, 1H), 4.91–4.76 (m, 1H), 4.59 (m, 2H), 4.49–4.27 (m, 1H), 3.06–2.83 (m, 2H), 1.65–1.49 (m, 2H), 1.46–1.38 (m, 2H), 1.34 (m, 1H), 1.23 (s, 1H), 0.93–0.80 (m, 6H); ^{13}C{^{1}H}NMR (100 MHz, DMSO-d_6) δ 172.0, 163.8, 142.2, 142.2, 142.2, 138.0, 135.0, 129.2, 129.2, 129.2, 129.2, 129.2, 129.2, 129.2, 129.2, 128.2, 128.2, 128.2, 128.2, 128.2, 128.2, 128.2, 128.1, 128.0, 128.0, 124.5, 122.4, 122.3, 119.8, 119.8, 110.6, 110.1, 74.6, 68.4, 61.2, 57.2, 54.1, 50.8, 31.0, 24.5, 23.0, 21.7, 21.6, 17.7; HRMS (ESI-TOF) m/z [M+H]$^+$ calcd for C$_{44}$H$_{41}$N$_6$O$_4$F$_2$: 755.3152, found 755.3152 [M+H]$^+$.

(R)-N-((S)-1-(((S)-1-cyano-2-(1H-imidazol-4-yl)ethyl)amino)-4-methyl-1-oxopentan-2-yl)-9,10-difluoro-3-methyl-7-oxo-2,3-dihydro-7H-[1,4]oxazino[2,3,4-ij]quinoline-6-carboxamide (6h). The synthetic method of 6a was adopted to synthesize 6h; pale white solid (0.045 g, 55%); $[\alpha]^{25}_D$: 4.71 (c=0.13, CHCl$_3$); mp: 115–120 °C; ^{1}H-NMR (400 MHz, CD$_3$OD) δ 8.76–8.55$_{rotamer}$ (m, 1H), 7.94$_{rotamer}$ (s, 1H), 7.16$_{rotamer}$ (m, 1H), 6.97$_{rotamer}$ (d, J=9.1 Hz, 1H), 4.61$_{rotamer}$ (m, 2H), 4.46$_{rotamer}$ (m, 1H), 4.41–4.35$_{rotamer}$ (m, 1H), 4.31$_{rotamer}$ (m, 1H), 3.15–2.84$_{rotamer}$ (m, 2H), 1.71–1.50$_{rotamer}$ (m, 2H), 1.47–1.42$_{rotamer}$ (m, 3H), 1.38$_{rotamer}$ (d, J=10.8 Hz, 1H), 0.84$_{rotamer}$ (m, 6H); ^{13}C{^{1}H}NMR (100 MHz, CD$_3$OD) δ 176.6, 175.1, 166.9, 156.5, 146.8, 146.3, 141.0, 136.6, 128.9, 127.0, 123.8, 118.7, 116.8, 111.3, 106.1, 70.8, 62.3, 56.8, 54.0, 42.8, 29.0, 26.1, 23.6, 22.2, 18.1; HRMS (ESI-TOF) m/z [M+H]$^+$ calcd for C$_{25}$H$_{27}$N$_6$O$_4$F$_2$: 513.2056, found 513.2050 [M+H]$^+$. *Note:* The residual solvent peak appear at. δ 3.97, 2.56, 1.88. Rotamer formation has been noted in related derivatives.[36]

(S)-N-((S)-1-cyano-2-(1-trityl-1H-imidazol-4-yl)ethyl)-4-methyl-2-(2-(phenylthio)acetamido)pentanamide (5i). The synthetic method of 5a was adopted to synthesize 5i; light yellow solid (0.195 g, 75%); $[\alpha]^{25}_D$: −7.90 (c=0.28, CHCl$_3$); mp: 70–75 °C; ^{1}H-NMR (400 MHz, DMSO-d_6) δ 8.91 (m, 1H), 8.32 (d, J=8.2 Hz, 1H), 7.46–7.36 (m, 9H), 7.29 (m, 5H), 7.16 (m, 1H), 7.07 (m, 6H), 6.86 (d, J=4.1 Hz, 1H), 5.02–4.87 (m, 1H), 4.28 (m, 1H), 3.81–3.55 (m, 2H), 3.05–2.82 (m, 2H), 1.53–1.29 (m, 3H), 0.83–0.68 (m, 6H); ^{13}C{^{1}H}NMR (100 MHz, DMSO-d_6) δ 171.9, 167.8, 142.2, 142.2, 142.2, 138.2, 136.0, 135.0, 129.2, 129.2, 129.2, 129.2, 129.2, 129.2, 129.2, 129.2, 128.9, 128.9, 128.2, 128.2, 128.2, 128.2, 128.1, 128.0, 127.9, 127.9, 125.8, 119.8, 119.1, 118.9, 74.6, 50.9, 40.8, 40.7, 36.1, 31.0, 24.0, 23.0, 21.3, 21.3; HRMS (ESI-TOF) m/z [M+H]$^+$ calcd for C$_{39}$H$_{40}$N$_5$O$_2$S: 642.2897, found 642.2890 [M+H]$^+$. *Note:* The residual ethyl acetate peak appear at. δ 4.05, 1.2.

(S)-N-((S)-1-cyano-2-(1H-imidazol-4-yl)ethyl)-4-methyl-2-(2-(phenylthio)acetamido)pentanamide (6i). The synthetic method of 6a was adopted to synthesize 6i; light yellow solid (0.054 g, 58%); $[\alpha]^{25}_D$: −9.41 (c=0.13, CHCl$_3$); mp: 145–150 °C; ^{1}H-NMR (400 MHz, CD$_3$OD) δ 7.55$_{rotamer}$ (d, J=4.8 Hz, 1H), 7.28$_{rotamer}$ (d, J=7.7 Hz, 2H), 7.19$_{rotamer}$ (t, J=7.5 Hz, 2H), 7.11$_{rotamer}$ (t, J=7.3 Hz, 1H), 6.78$_{rotamer}$ (d, J=8.5 Hz, 1H), 4.49$_{rotamer}$ (m, 1H), 4.21–3.95$_{rotamer}$ (m, 1H), 3.56$_{rotamer}$ (m, 2H), 3.12–2.67$_{rotamer}$ (m, 2H), 1.41–1.18$_{rotamer}$ (m, 3H), 0.78–

Research Article

0.62$_{rotamer}$ (m, 6H); ^{13}C{^{1}H}NMR (100 MHz, CD$_3$OD) δ 172.0, 136.4, 136.4, 134.4, 130.7, 130.2, 130.2, 130.2, 130.2, 127.9, 118.6, 54.3, 53.7, 41.4, 38.4, 30.0, 25.6, 23.5, 21.7, 21.7; HRMS (ESI-TOF) m/z [M+H]$^+$ calcd for C$_{20}$H$_{26}$N$_5$O$_2$S: 400.1802, found 400.1804 [M+H]$^+$. *Note:* The residual solvent peak appear at. δ 1.85. Rotamer formation has been noted in related derivatives.[36]

In-vitro studies: The inhibitors were dissolved in DMSO and stored at −20°C until further use. The cytotoxicity and antiviral assays were performed using different concentrations to determine CC$_{50}$ and EC$_{50}$ values respectively, using standard experimental procedures.

In-vitro evaluation of cell cytotoxicity of candidate drugs (inhibitors 6c, 6f and 6i): Vero cells were seeded in a 96-well culture plate with DMEM containing 10% FBS, incubated for 24 hrs (37°C with 5% CO$_2$) until it reaches ~80 to 90% confluency. Different concentrations of (6.25 μM, 12.5 μM, 25 μM, 50 μM, 100 μM and 200 μM) of the candidate drug molecules (6c, 6f and 6i) along with DMSO control were added to the cells to determine the cytotoxicity for 24 hrs. After 24 hrs post-incubation, the media containing the inhibitor molecules was removed and MTT solution (1 mg/mL) was added, and the cells were incubated at 37°C, 5% CO$_2$ for 2 hrs. After the incubation, the MTT solution was removed and DMSO (100 μL) was added and incubated at 37°C for 30 mins with 5% CO$_2$ to dissolve the formazan crystals.[38] Post incubation, the formazan color absorbance was measured at 570 nm in BioTek Microplate Reader.

Anti-COVID activity of candidate drugs (inhibitors 6c, 6f and 6i): Among the inhibitors tested 6c, 6f and 6i were selected for the anti-COVID screening based on their docking scores. The viral titer was adjusted to ensure only viral replication without cytolysis. The screening procedures were performed in the BSL-3 facility. The selected inhibitors (6c, 6f and 6i) were tested against the SARS-CoV-2 virus (A3i clade) with different concentrations (0.1 μM to 10 μM for 6i and 0.1 μM to 20 μM for 6f and from 0.1 μM to 15 μM for 6c). Molnupiravir was used as the assay control drug.[34] Briefly, Vero cells after reaching confluency of 80–90% in a 96-well plate were preincubated (Priming) with 200 μL (three replicates) of each inhibitor along with Molnupiravir (Assay Control Drug). The respective candidate inhibitors were dissolved in DMEM supplemented with 10% FBS and incubated at 37°C for 2 hrs. Post priming, the cell culture media was removed and a known titer of the SARS-CoV-2 virus, along with selected inhibitors was used for infection (50 μL). The infection was carried out in serum free media for 3 hrs. Post-infection, (PI), the media containing the virus was removed and fresh media containing the inhibitor molecules (6c, 6f and 6i) along with Molnupiravir (200 μL) was added to the cells and maintained at 37°C with 5% CO$_2$ for 72 hrs.

RNA isolation and RT-qPCR evaluation of viral copies: 72 hrs post-incubation, the supernatants were collected in 96 Deep well plates (KingFisherTMThermo Scientific) and lysis buffer, comprising of 260 μL, MagMAX™ Viral/Pathogen Binding Solution; 10 μL, MVP-II Binding Beads; 5 μL, MagMAXTM Viral/Pathogen Proteinase-K, was added to the collected supernatant (200 μL). The viral RNA isolation was performed in the automated KingFisher Flex (version 1.01, Thermo Scientific) using Mag-MaxTM Viral/Pathogen Extraction Kit (Applied Bio-systems, Thermofisher) according to the manufacturer's instructions. The obtained RNA was stored at −80°C until further use.

The SARS-CoV-2 viral load was quantified using specific primers by RT-qPCR (QuantStudio™5 Real-Time PCR - Applied Biosystems). One-step RT-qPCR Kit (Meril Diagnostics Pvt. Ltd) was used according to the manufacturer's instructions. The kit contains real-time PCR amplification reagents which detect the SARS-CoV-2 viral Open Reading Frame (ORF1ab)-gene detected by the FAM channel, Nucleoprotein (N)-gene detected by the HEX channel and the host endogenous RNaseP-gene (Internal Control gene) detected by the ROX channel.

The N-gene amplification (Ct) was considered to enumerate the viral particles in the experimental groups using the lab-established linear regression equation.[29] The Log Viral particles in the control and experimental group were extrapolated from the linear regression equation obtained from a semi-log standard graph which is plotted by isolating the RNA from quantified by performing the RT-qPCR. The log EC$_{50}$ for the inhibitor molecules was calculated in GraphPad Prism, version 8.4.2 software as per the established protocol.[39,40]

Statistical Analysis: The data analysis and graphs were generated using GraphPad Prism, version 8.4.2 software. All the experiments were performed in triplicates. The values were represented as Mean ± SD.

Ethical approval: The SARS-CoV2 study was performed in CSIR-Centre for Cellular and Molecular Biology, Hyderabad with the approval of the Institutional BioSafety Committee.

Computational Details: In the first step, the crystal structure of the 3CL^{pro} or M^{pro} protease of the SARS-CoV-2 (PDB: 7ALH)[41] at 1.65 Å resolution was equilibrated through all-atom MD simulations in an explicit water solvent. On the other hand, the structures of all inhibitors were optimized at the B3LYP/6-311G (d,p) level[42,43] using the Gaussian 16 program. These optimizations were carried out in explicit water solvent using the polarizable continuum model (IEFPCM).[44] The empirical dispersion interactions were also incorporated using the GD3BJ[45] dispersion functional as implemented in Gaussian 16. The initial structures of enzyme-inhibitor complexes were built through docking of DFT-optimized inhibitors on the MD equilibrated crystal structure of Mpro utilizing the AutoDockTools 4.2.[46] The two lowest energy poses provided by the docking procedure in each case were subsequently subjected to 200 ns all-atom MD simulations using the GROMACS 2020.2 program.[47] In these simulations, the protein M^{pro} was treated using the Amber 99-ILDN forcefield,[48] while the solvent was treated using the TIP3P water model.[49] The forcefield parameters of inhibitors were created using the ANTECHAMBER[50] and Generalized Amber Force Field (GAFF)[51] tools available in the AMBERTOOLS program. The Coulombic and Van der Waals (VDW) potentials were computed using the Particle Mesh Ewald (PME) method[52] with a cutoff of 1.2 Å. The relevant constraints were treated using LINCS algorithm.[53] The Velocity rescale temperature[54] and Berendsen pressure coupling[55] models were employed for the production MD runs. Several sodium and chloride ions were added to neutralize the solvated system. The binding energies of the inhibitors were computed using the Molecular Mechanics – Poisson Boltzmann Surface Area (MM-PBSA) method[56] the root-mean-square deviation (RMSD) of these simulations showed that they were well equilibrated within the time frame of simulations (Figure 3, *supp. info.*).

Docking Protocol Validation: Docking protocol validation was performed with the x-ray structure of M^{pro} protease co-crystallized with the covalent inhibitor N3 (PDB ID: 6LU7). The co-crystallized ligand was removed and the inhibitor 6i was docked on to the protease. The lowest energy poses were analyzed and compared to poses recorded from the original docking protocol (Figure 2, *supp. Info.*).

Author Contributions

G. J. Sanjayan and N. V. Gone conceived and designed the experiments, analyzed the data and wrote the manuscript. K. K. Bokara, M. G. Enayathullah and J. Thomas performed the in-vitro assay and wrote the paper. R. Prabhakar and P. Rathee contributed to the molecular docking studies and wrote the manuscript.

Conflict of Interests

The authors declare no conflict of interest.

Data Availability Statement

The data that support the findings of this study are available in the supplementary material of this article.

[1] "WHO Coronavirus (COVID-19) Dashboard | WHO Coronavirus (COVID-19) Dashboard with Vaccination Data," can be found under https://covid19.who.int/.

[2] N. M. Anand, D. H. Liya, A. K. Pradhan, N. Tayal, A. Bansal, S. Donakonda, A. K. Jainarayanan, PLoS One 2021, 16, 1–21.

[3] L. Zhang, D. Lin, X. Sun, U. Curth, C. Drosten, L. Sauerhering, S. Becker, K. Rox, R. Hilgenfeld, Science 2020, 368, 409–412.

[4] C. S. Dampalla, Y. Kim, N. Bickmeier, A. D. Rathnayake, H. N. Nguyen, J. Zheng, M. M. Kashipathy, M. A. Baird, K. P. Battaile, S. Lovell, S. Perlman, K. O. Chang, W. C. Groutas, J. Med. Chem. 2021, 64, 10047–10058.

[5] X. R. Ma, Y. R. Alugubelli, Y. Ma, E. C. Vatansever, D. A. Scott, Y. Qiao, G. Yu, S. Xu, W. R. Liu, ChemMedChem 2022, 17, 1–8.

[6] M. D. Sacco, C. Ma, P. Lagarias, A. Gao, J. A. Townsend, X. Meng, P. Dube, X. Zhang, Y. Hu, N. Kitamura, B. Hurst, B. Tarbet, M. T. Marty, A. Kolocouris, Y. Xiang, Y. Chen, J. Wang, Sci. Adv. 2020, 6, 1–15.

[7] T. Pillaiyar, M. Manickam, V. Namasivayam, Y. Hayashi, S. H. Jung, J. Med. Chem. 2016, 59, 6595–6628.

[8] D. Bojadzic, O. Alcazar, J. Chen, S. T. Chuang, J. M. C. Capcha, L. A. Shehadeh, P. Buchwald, ACS Infect. Dis. 2021, 7, 1519–1534.

[9] T. Muramatsu, C. Takemoto, Y. T. Kim, H. Wang, W. Nishii, T. Terada, M. Shirouzu, S. Yokoyama, Proc. Natl. Acad. Sci. USA 2016, 113, 12997–13002.

[10] A. D. Rathnayake, J. Zheng, Y. Kim, K. Dinali Perera, S. Mackin, D. K. Meyerholz, M. M. Kashipathy, K. P. Battaile, S. Lovell, S. Perlman, W. C. Groutas, K. O. Chang, Sci. Transl. Med. 2020, 12, 1–11.

[11] Y. Liu, C. Liang, L. Xin, X. Ren, L. Tian, X. Ju, H. Li, Y. Wang, Q. Zhao, H. Liu, W. Cao, X. Xie, D. Zhang, Y. Wang, Y. Jian, Eur. J. Med. Chem. 2020, 206, 112711.

[12] A. Citarella, A. Scala, A. Piperno, N. Micale, Biomol. Eng. 2021, 11, 607.

[13] J. Qiao, Y. S. Li, R. Zeng, F. L. Liu, R. H. Luo, C. Huang, Y. F. Wang, J. Zhang, B. Quan, C. Shen, X. Mao, X. Liu, W. Sun, W. Yang, X. Ni, K. Wang, L. Xu, Z. L. Duan, Q. C. Zou, H. L. Zhang, W. Qu, Y. H. P. Long, M. H. Li, R. C. Yang, X. Liu, J. You, Y. Zhou, R. Yao, W. P. Li, J. M. Liu, P. Chen, Y. Liu, G. F. Lin, X. Yang, J. Zou, L. Li, Y. Hu, G. W. Lu, W. M. Li, Y. Q. Wei, Y. T. Zheng, J. Lei, S. Yang, Science 2021, 371, 1374–1378.

[14] S. Mondal, Y. Chen, G. J. Lockbaum, S. Sen, S. Chaudhuri, A. C. Reyes, J. M. Lee, A. N. Kaur, N. Sultana, M. D. Cameron, S. A. Shaffer, C. A. Schiffer, K. A. Fitzgerald, P. R. Thompson, J. Am. Chem. Soc. 2022, 144, 21035–21045.

[15] B. Bai, E. Arutyunova, M. B. Khan, J. Lu, M. A. Joyce, H. A. Saffran, J. A. Shields, A. S. Kandadai, A. Belovodskiy, M. Hena, W. Vuong, T. Lamer, H. S. Young, J. C. Vederas, D. L. Tyrrell, M. J. Lemieux, J. A. Nieman, RSC Med. Chem. 2021, 12, 1722–1730.

[16] D. Shcherbakov, D. Baev, M. Kalinin, A. Dalinger, V. Chirkova, S. Belenkaya, A. Khvostov, D. Krut'Ko, A. Medved'Ko, E. Volosnikova, E. Sharlaeva, D. Shanshin, T. Tolstikova, O. Yarovaya, R. Maksyutov, N. Salakhutdinov, S. Vatsadze, ACS Med. Chem. Lett. 2022, 13, 140–147.

[17] L. Wang, Z. Yu, S. Wang, Z. Guo, Q. Sun, L. Lai, Eur. J. Med. Chem. 2022, 244, 114803.

[18] K. Akaji, H. Konno, Molecules 2020, 25, 3920.

[19] C. S. B. Chia, W. Xu, P. S. Ng, ChemMedChem 2022, 17, 1–12.

[20] J. Breidenbach, C. Lemke, T. Pillaiyar, L. Schäkel, G. A. Hamwi, M. Diett, R. Gedschold, N. Geiger, V. Lopez, S. Mirza, V. Namasivayam, A. C. Schiedel, K. Sylvester, D. Thimm, C. Vielmuth, L. P. Vu, M. Zyulina, J. Bodem, M. Gütschow, C. E. Müller, Angew. Chem. Int. Ed. 2021, 60, 10423–10429.

[21] C. Ma, Z. Xia, M. D. Sacco, Y. Hu, J. A. Townsend, X. Meng, J. Choza, H. Tan, J. Jang, M. V. Gongora, X. Zhang, F. Zhang, Y. Xiang, M. T. Marty, Y. Chen, J. Wang, J. Am. Chem. Soc. 2021, 143, 20697–20709.

[22] S. Iketani, F. Forouhar, H. Liu, S. J. Hong, F. Y. Lin, M. S. Nair, A. Zask, Y. Huang, L. Xing, B. R. Stockwell, A. Chavez, D. D. Ho, Nat. Commun. 2021, 12, 1–7.

[23] D. R. Owen, C. M. N. Allerton, A. S. Anderson, L. Aschenbrenner, M. Avery, S. Berritt, B. Boras, R. D. Cardin, A. Carlo, K. J. Coffman, A. Dantonio, L. Di, H. Eng, R. Ferre, K. S. Gajiwala, S. A. Gibson, S. E. Greasley, B. L. Hurst, E. P. Kadar, A. S. Kalgutkar, J. C. Lee, J. Lee, W. Liu, S. W. Mason, S. Noell, J. J. Novak, R. S. Obach, K. Ogilvie, N. C. Patel, M. Pettersson, D. K. Rai, M. R. Reese, M. F. Sammons, J. G. Sathish, R. S. P. Singh, C. M. Steppan, A. E. Stewart, J. B. Tuttle, L. Updyke, P. R. Verhoest, Science 2021, 374, 1586–1593.

[24] C. P. Chuck, C. Chen, Z. Ke, D. C. C. Wan, H. F. Chow, K. B. Wong, Eur. J. Med. Chem. 2013, 59, 1–6.

[25] R. L. Hoffman, R. S. Kania, M. A. Brothers, J. F. Davies, R. A. Ferre, K. S. Gajiwala, M. He, R. J. Hogan, K. Kozminski, L. Y. Li, J. W. Lockner, J. Lou, M. T. Marra, L. J. Mitchell, B. W. Murray, J. A. Nieman, S. Noell, S. P. Planken, T. Rowe, K. Ryan, G. J. Smith, J. E. Solowiej, C. M. Steppan, B. Taggart, J. Med. Chem. 2020, 63, 12725–12747.

[26] D. Y. Duveau, C. J. Thomas, ACS Pharmacol. Transl. Sci. 2022, 5, 445–447.

[27] L. Vangeel, W. Chiu, S. D. Jonghe, P. Maes, B. Slechten, J. Raymenants, E. André, P. Leyssen, J. Neyts, D. Jochmans, Antiviral Res. 2022, 198, 105252.

[28] While this work was in progress, we came across a patent reporting histidine alpha nitrile motif. L. D. Arnold, A. Jennings, W. Keung. Pardes Biosciences, Inc., inhibitors of cysteine proteases and methods of use thereof. United States Patent US 11,124,497 B1. 2021 Sep 21.

[29] W. Dai, B. Zhang, X. M. Jiang, H. Su, J. Li, Y. Zhao, X. Xie, Z. Jin, J. Peng, F. Liu, C. Li, Y. Li, F. Bai, H. Wang, X. Cheng, X. Cen, S. Hu, X. Yang, J. Wang, X. Liu, G. Xiao, H. Jiang, Z. Rao, L. K. Zhang, Y. Xu, H. Yang, H. Liu, Science 2020, 368, 1331–1335.

[30] G. L. Monica, A. Bono, A. Lauria, A. Martorana, J. Med. Chem. 2022, 65, 12500–12534.

[31] Several short hydrophobic peptides featuring diverse war head groups targeting 3CLᵖʳᵒ and PLᵖʳᵒ of SARS-CoV-2 have been reported recently. Z. Xia, M. Sacco, Y. Hu, C. Ma, X. Meng, F. Zhang, T. Szeto, Y. Xiang, Y. Chen, J. Wang, ACS Pharmacol. Transl. Sci. 2021, 4, 1408–1421.

[32] Faridoor, R. Ng, G. Zhang, J. J. Li, Med. Chem. Res. 2023, 32, 1039–1062.

[33] K. Akaji, H. Konno, H. Mitsui, K. Teruya, Y. Shimamoto, Y. Hattori, T. Ozaki, M. Kusunoki, A. Sanjoh, J. Med. Chem. 2011, 54, 7962–7973.

[34] S. Singla, S. Goyal, Bull. Natl. Res. Cent. 2022, 46, 62.

[35] J. Kyte, R. F. Doolittle, J. Mol. Biol. 1982, 157, 105–132.

[36] S. Li, M. Hong, J. Am. Chem. Soc. 2011, 133, 1534–1544.

[37] V. V. E. Ramesh, G. Priya, A. S. Kotmale, R. G. Gonnade, P. R. Rajamohanan, G. J. Sanjayan, Chem. Commun. 2012, 48, 11205–11207.

[38] S. Vijayarathna, S. Sasidharan, *Asian. Pac. J. Trop. Biomed.* **2012**, *2*, 826–829.

[39] M. Chauhan, V. K. Bhardwaj, A. Kumar, V. Kumar, P. Kumar, M. G. Enayathullah, J. Thomas, J. George, B. K. Kumar, R. Purohit, A. Kumar, S. Kumar, *Sci. Rep.* **2022**, *12*, 13146.

[40] M. G. Enayathullah, Y. Parekh, S. Banu, S. Ram, R. Nagaraj, B. K. Kumar, M. M. Idris, *Sci. Rep.* **2022**, *12*, 3446.

[41] E. Costanzi, M. Kuzikov, F. Esposito, S. Albani, N. Demitri, B. Giabbai, M. Camasta, E. Tramontano, G. Rossetti, A. Zaliani, P. Storici, *Int. J. Mol. Sci.* **2021**, *22*, 11779.

[42] A. D. Becke, *J. Chem. Phys.* **1993**, *98*, 5648–56452.

[43] K. Raghavachari, J. S. Binkley, R. Seeger, J. A. Pople, *J. Chem. Phys.* **1980**, *72*, 650–654.

[44] G. Scalmani, M. J. Frisch, *J. Chem. Phys.* **2010**, *132*, 114110.

[45] S. Grimme, S. Ehrlich, L. Goerigk, *J. Comput. Chem.* **2011**, *32*, 1456–1465.

[46] G. M. Morris, R. Huey, W. Lindstrom, M. F. Sanner, R. K. Belew, D. S. Goodsell, A. J. Olson, *J. Comput. Chem.* **2010**, *30*, 2785–2791.

[47] H. Bekker, J. C. H. Berendsen, E. J. Dijkstra, S. Achterop, R. Drunen, D. Spoel, A. Sijbers, H. Keegstra, M. K. R. Renardus, *GROMACS - a parallel computer for moleculardynamics simulations*, Physics computing 92, World Scientific, Singapore, **1993**, pp. 252–256.

[48] K. L. Larsen, S. Piana, K. Palmo, P. Maragakis, J. L. Klepeis, R. O. Dror, D. E. Shaw, *Proteins* **2010**, *78*, 1950–1958.

[49] W. L. Jorgensen, J. Chandrasekhar, J. D. Madura, R. W. Impey, M. L. Klein, *J. Chem. Phys.* **1983**, *79*, 926–935.

[50] J. Wang, W. Wang, P. A. Kollman, D. A. Case, *J. Am. Chem. Soc.* **2001**, *222*, U403.

[51] J. Wang, R. M. Wolf, J. W. Caldwell, P. A. Kollman, D. A. Case, *J. Comput. Chem.* **2004**, *25*, 1157–1174.

[52] D. Tom, D. York, L. Pedersen, *J. Chem. Phys.* **1993**, *98*, 10089–10092.

[53] H. Berk, H. Bekker, H. J. Berendsen, J. G. Fraaije, *J. Comput. Chem.* **1997**, *18*, 1463–1472.

[54] G. Bussi, D. Donadio, M. Parrinello, *J. Chem. Phys.* **2007**, *126*, 014101.

[55] H. J. C. Berendsen, J. P. M. Postma, A. DiNola, J. R. Haak, *J. Chem. Phys.* **1984**, *81*, 3684–3690.

[56] M. S. Valdés-Tresanco, M. E. Valdés-Tresanco, P. A. Valiente, E. Moreno, *J. Chem. Theory Comput.* **2021**, *17*, 6281–6291.